A Computational Tool to Interpret the Bulk Composition of Solid Exoplanets based on Mass and Radius Measurements

LI ZENG,[1] AND S. SEAGER[1,2]

ABSTRACT. The prospects for finding transiting exoplanets in the range of a few to 20 $M_\oplus$ is growing rapidly with both ground-based and spaced-based efforts. We describe a publically available computer code to compute and quantify the compositional ambiguities for differentiated solid exoplanets with a measured mass and radius, including the mass and radius uncertainties.

1. INTRODUCTION

Over 250 extrasolar planets are known to orbit nearby main sequence stars. Among these include over a dozen exoplanets with minimum masses below 22 $M_\oplus$ and several with minimum masses less than 10 $M_\oplus$. Of key interest are transiting planets with measured masses and radii, which can be used to constrain the planet's interior bulk composition. The relationship between mass and radius for solid exoplanets has hence received much attention in the last few years (Valencia et al. 2006; Fortney et al. 2007; Seager et al. 2007; Selsis et al. 2007; Sotin et al. 2007). The recent activity builds on much earlier work (Zapolsky & Salpeter 1969; Stevenson 1982), with improvements on the equations of state and treatment of different mantle and core compositions to varying degrees of complexity.

Unlike for the solar system planets, we have no access to the gravitational moments of exoplanets. Hence the density distribution in the interior is unknown and this leads to an ambiguity, or degeneracy, in the interior composition for an exoplanet of a fixed mass and radius. One way to capture the degeneracies of exoplanet interior composition is using ternary diagrams (introduced to exoplanet interiors by Valencia et al. 2007).

We adopt the idea of using ternary diagrams to quantify the compositional uncertainty in exoplanets. The planet mass and radius are the observed quantities and therefore we focus solely on ternary diagrams for a planet of fixed mass and fixed radius (c.f. Valencia et al. 2007). We compute ternary diagrams for solid exoplanets ranging in mass from 0.5 to 20 $M_\oplus$. We furthermore explain the behavior of the mass-radius curves in two and three dimensions. We also present a description of our publicly available computer code to compute fixed mass-radius ternary diagrams, including the observational uncertainties.

[1] Department of Physics, Massachusetts Institute of Technology, Cambridge, MA

[2] Department of Earth, Atmospheric and Planetary Sciences, Massachusetts Institute of Technology, Cambridge, MA

2. COMPUTER MODEL

2.1. Background and Equations

We begin by assuming the major components of a solid exoplanet are limited to an iron core, a silicate mantle, and a water–ice outer layer. In other words, we assume the interior of the planet is differentiated with the denser materials interior to the less dense materials. We further assume each layer to be homogeneous in its composition.

We can then model the interior of a solid exoplanet by using:

1.the equation for mass of a spherical shell

$$\frac{dm(r)}{dr} = 4\pi r^2 \rho(r),$$ (1)

where $m(r)$ is the mass included in radius r and $\rho(r)$ is the density at radius r;

2.the equation for hydrostatic equilibrium

$$\frac{dP(r)}{dr} = \frac{-Gm(r)\rho(r)}{r^2},$$ (2)

where $P(r)$ is the pressure at radius r; and

3.the equation of state (EOS) that relates P and ρ.

The EOS is different for each different material. We used Fe (ϵ) for the planet core, $MgSiO_3$ perovskite for the silicate mantle, and water-ice VII, VIII, and X for the water–ice outer layer. See Seager et al. (2007) for a detailed discussion of the EOSs including their source. The temperature has little effect on the EOS especially in the high pressure regime (Seager et al. 2007); we ignore the temperature dependence of the EOS. This simplifies the equations and their solution, while enabling a relatively accurate analysis.

In this problem, we have five variables:

1. the iron mass fraction (α);
2. the silicate mass fraction (β);
3. the water–ice mass fraction (γ);

4. the total mass of the planet (M_p); and
5. the mean radius of the planet (R_p).

The variables α, β, and γ are not independent of each other. Based on the assumption that the planet only consists of iron, silicate, and water we have: $\alpha + \beta + \gamma = 1$, which can also be expressed as $\gamma = 1 - \alpha - \beta$. We therefore have four variables: α, β, M_p, and R_p. Given any three of these variables, we can determine the fourth variable uniquely. We can also see that given M_p and R_p, there is a relationship between α and β. There is not a single value of α and β that produces a given M_p and R_p. Instead, there are infinite pairs of α and β that give the same M_p and R_p, and we call this a degeneracy in the interior composition.

2.2. Algorithm for Solving the Differential Equations

Our program integrates from the surface $r = R_p$ inward to the center of the planet. The outer boundary condition is $m(R_p) = M_p$ and $P(R_p) = 0$. That is, at the surface, the mass is the specified total planet mass and the pressure is approximately zero.

We aim to interpret observations of a planet of a given mass and radius. We therefore choose to integrate inwards instead of outwards based upon the known parameters of the planet (M_p, R_p, and $P(R_p)$). The independent variable is r, decreasing from $r = R_p$ to $r = 0$. The interior boundary condition is $m(r) = 0$ at $r = 0$. Typically, when integrating $m(r)$, m does not equal zero at $r = 0$. We therefore must iterate, tuning the mass fraction of each layer until $m = 0$ and $r = 0$ is reached.

Given a single M_p and R_p the computer program finds all possible combinations of α, β, and $\gamma(= 1 - \alpha - \beta)$ that give the same planet mass and radius. The program begins with a chosen value of α, and then takes a guess of β. Next, the computer program integrates differential equations (1) and (2) using the above boundary conditions to find the value of the planet radius. By comparing this radius to the desired R_p, the computer program tunes the value for β using the bisection method. This process is repeated several times, until β is found to a satisfactory accuracy of $1/1000$. By varying α within the range of 0 to 1, we can get all possible combinations of α and β, which produce a specific M_p and R_p.

2.3. Algorithm for Generating a Database of $M_p = 0.5$–$20\ M_\oplus$

M_p and R_p are observed parameters and one usually wants to find the corresponding allowed α and β. For a range of M_p and R_p—corresponding to observational uncertainties—it can be very time consuming to use the first algorithm described in § 2.2. We therefore generate a database that is a discrete representation of the relation $R_p = R_p(\alpha, \beta, M_p)$. Figure 1 illustrates the 4D database.

This database is a 3D array that contains the data of R_p corresponding to each combination of α and β (0 to 1 with 1% spacing) and $M_\oplus$ (ranging from 0.5 to 20 $M_\oplus$ with 0.25 $M_\oplus$ spacing). The database can be used via linear interpolation
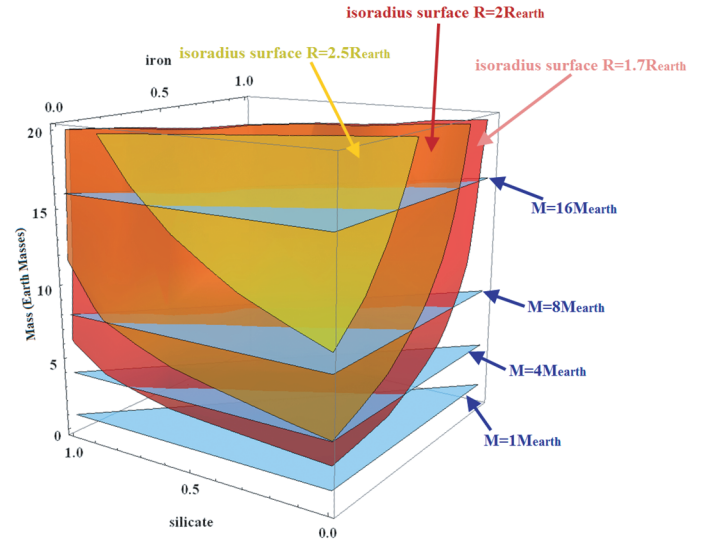

FIG. 1.—3D representation of planet mass, planet radius, and composition expressed as mass fractions of iron (α) and silicate (β). The x-axis is the iron mass fraction and the y-axis is the silicate mass fraction. The water mass fraction comes from $\alpha + \beta + \gamma = 1$. The z-axis is the total planet mass in Earth masses. The planet radius is not indicated, except by three separate surfaces of constant radius. An isomass and isoradius surface intersect with a curve in a 2D iron mass fraction vs. silicate mass fraction Cartesian diagram (Fig. 2).

to find R_p for any given M_p, α, and β. A conservative estimate of the fractional error in the database interpolation is $1/1000$. For the same range of M_p and R_p, interpolation in the database is about 45 times faster than solving the differential equations.

To generate a database of all values of α, β, and R_p for M_p ranging from 0.5 to 20 $M_\oplus$. Given M_p, α, and β, this algorithm also integrates from the surface inward to $r = 0$ and $m(r) = 0$ to find R_p. In contrast to the first algorithm (which solves for a given M_p and R_p), a single integration in radius results in the desired solution of R_p, for a given M_p, α, and β. In other words there is no iteration required, making this algorithm much more efficient.

2.4. Instructions for Downloading and Using the Code

The code is based in MATLAB and can be downloaded.[3] If using this computer code please cite this paper and also Seager et al. (2007).

We have made two different codes available. The codes have the same output, but the first is based on a differential equation solver (§ 2.2) and the second code is based on interpolation of the large database (§ 2.3). For the codes, the planet mass must be in the range 0.5–20 $M_\oplus$. The inputs to the codes are: the planet mass in Earth masses (M_p), the planet mass uncertainty in Earth masses (σ_{M_p}), the planet radius in Earth radii (R_p), and the

---

[3] To download computer code, see http://web.mit.edu/zengli/www/ under "Research Field" or from http://seagerexoplanets.mit.edu/research/interiors.html.
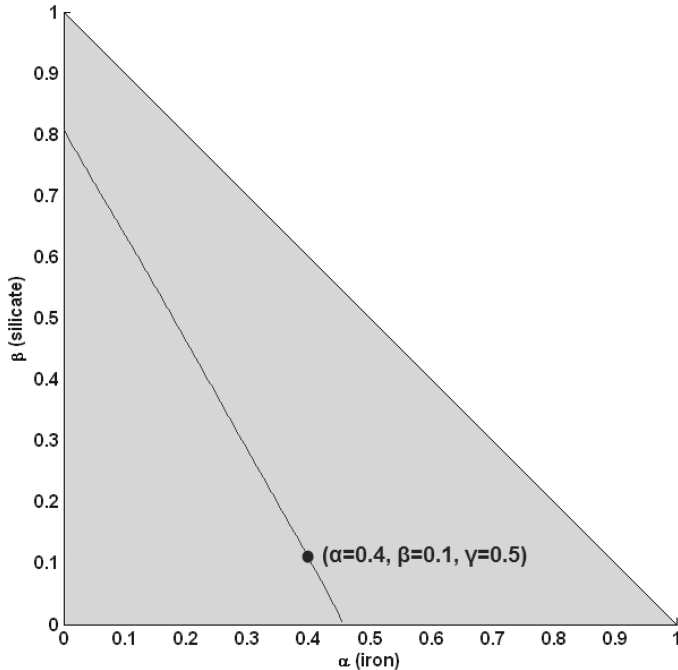
FIG. 2.—Cartesian diagram for silicate mass fraction (β) vs. iron mass fraction (α) for a planet with $M_p = 4\ M_\oplus$ and $R_p = 1.7\ R_\oplus$ (note that the water mass fraction $\gamma = 0.4$ since $\gamma = 1 - \alpha - \beta$). A planet of a fixed internal composition is represented as a point in the gray shaded region (only compositions in the gray shaded region are allowed). With a given planet mass and radius there is not a unique interior composition; the allowed compositions are described by the curve. The curve originates from the intersection of the isomass surface and the isoradius surface in the 3D representation (Fig. 1).

planet radius uncertainty in Earth radii (σ_{R_p}). The values $\sigma_{M_p} = 0$ and $\sigma_{R_p} = 0$ are allowed. If the combination of input values M_p and R_p are unphysical, the code will return an error.

ExoterDE($M_p, \sigma_{M_p}, R_p, \sigma_{R_p}$). This code solves the two differential equations described in § 2.1. This code consists of three subroutines (each of which must be downloaded) that are automatically called by the above command. The first subroutine is the differential equation solver, which also reads the equations of state. The second subroutine contains the actual differential equations. The third subroutine plots the ternary diagrams; this subroutine calls a ternary diagram plotting routine [4] that plots a single line for each of the 1, 2, and 3 σ contour lines (see § 4.1). An example from this code is shown in Figure 4.

ExoterDB($M_p, \sigma_{M_p}, R_p, \sigma_{R_p}$). This code reads in the database of M_p, R_p, and fractional composition (α and β). The output is a ternary diagram, shaded throughout the 1, 2, and 3 σ contour curves. This subroutine uses the same ternary diagram plotting routine as described above.

---

[4] See http://www.mathworks.com/matlabcentral/fileexchange/loadFile.do?objectId=7210&objectType=file for more information.

The differential equation solver ExoterDE is much slower than the database extracter ExoterDB. In principle, ExoterDE is more accurate than ExoterDB.

3. DATA DISPLAY

3.1. 2D Cartesian Diagram

For a given M_p and R_p we want to know the interior composition of the relative mass fraction of the three components. There are three variables we have solved for α, β, and γ, but only two of them are independent (since $\gamma = 1 - \alpha - \beta$). Therefore points on a 2D diagram can describe all the possible combinations of α, β, and γ for a given M_p and R_p. We show such a solution in Figure 2. We note that $0 \leq \alpha \leq 1$, $0 \leq \beta \leq 1$, and $\alpha + \beta \leq 1$, and therefore, not every point in the 2D plane will correspond to a set of α, β, and γ. Only the points that are in a right-angled triangular region will represent the set of allowed solutions.

3.2. Ternary Diagram

Ternary diagrams to describe the interior composition of exoplanets were introduced by Valencia et al. (2007). In a ternary diagram, α, β, and γ are each one axis of an equilateral triangle. Although γ is extraneous, the ternary diagram is useful because it is more intuitive to see the three components of the planet interior (in a symmetric way) compared to a 2D Cartesian diagram with only two of the components. Figure 3 shows how to read a ternary diagram.

3.3. Relationship Between the 3D and 2D Cartesian Diagrams and the Ternary Diagram

To explain the full origin of a curve on the ternary diagram we start with the 3D Cartesian diagram with all solutions of M_p, R_p, and composition (in terms of α and β), as shown in Figure 1. We take an isoradius and isomass surface as shown in Figure 1. As an example, in Figure 1 the red surface is the isoradius surface of $R_p = 1.7\ R_\oplus$ and one of the blue colored planes is the isomass surface of $M_p = 4\ M_\oplus$. These two surfaces intersect each other and result in a curve. This curve can be projected vertically to the x–y plane, which is the isomass plane. We therefore have a (isoradius and isomass) curve on the isomass plane. This curve is shown in Figure 2 in a Cartesian diagram.

The Cartesian and ternary diagrams are two different ways to represent the same information. There exists a linear coordinate transformation between the two. That means if a function is a straight line appearing in the 2D Cartesian diagram, it will still be a straight line in the ternary diagram.

The transformation from 2D Cartesian coordinates to the ternary diagram coordinates is
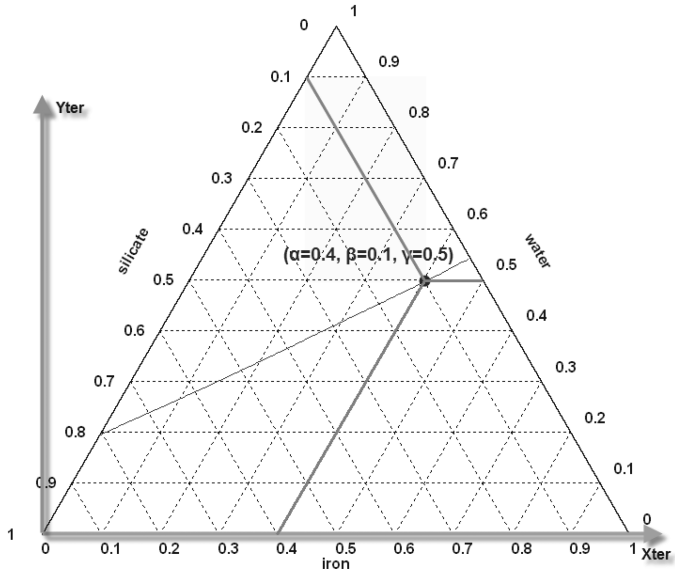
$$x_{\text{ternary}} = \frac{1}{2}(1 + x - y), \tag{3}$$

FIG. 3.—Ternary diagram for a planet of the same mass and radius as shown in the corresponding Cartesian diagram in Figure 2. The light gray x- and y-axes are shown to illustrate how this ternary diagram relates to a Cartesian diagram; x_{ternary} and y_{ternary} are the coordinates transformed from the Cartesian coordinates. (See § 3.3 for the conversion equations.) Any point on the curve is a possible combination of iron, silicate, and water that will result in a planet with $M_p = 4\ M_\oplus$ and $R_p = 1.7\ R_\oplus$. This Figure also illustrates how to read a ternary diagram. Consider a triangle oriented such that the value 1 (of a given material) is at the triangle's apex. The mass fraction of that given material can be read off of a horizontal line that is perpendicular to the line connecting the triangle's apex with the triangle base.

$$y_{\text{ternary}} = \frac{\sqrt{3}}{2}(1 - x - y). \tag{4}$$

Here x and y are the coordinates of a point in a 2D Cartesian diagram, the x_{ternary} and y_{ternary} are the coordinates of the point in ternary diagram in the Cartesian grid variables. Figure 3 shows the same $R_p = 1.7\ R_\oplus$, $M_p = 4\ M_\oplus$ curve represented by a ternary diagram.

4. RESULTS AND DISCUSSION

4.1. Observational Uncertainties

Real planet mass and radius measurements have uncertainties. The planet mass and radius uncertainties are typically 5 to 10% (e.g., Selsis et al. 2007), and even smaller for the most favorable targets. We now present examples of ternary diagrams that include the mass and radius uncertainties.

We consider uncertainties of 1, 2, and 3 standard deviations (σ) from the measured value. See Figures 4 and 5. In more detail, the uncertainty in composition on the ternary diagram is

$$\sigma_{\text{comp}} = \sqrt{(\sigma_{\text{comp}M})^2 + (\sigma_{\text{comp}R})^2}, \tag{5}$$

where comp refers to composition and comp$M$ and comp$R$ refer to composition uncertainties caused by the planet mass and radius uncertainty, respectively. Here we have assumed that the uncertainties in mass and radius are independent from each other and have assumed the linearity of the superposition of small uncertainties.

Figure 4 shows a planet with $M_p = 10 \pm 0.5\ M_\oplus$ and $R_p = 2 \pm 0.1\ M_\oplus$. We see that taking the 3 σ limit, almost the entire ternary diagram is filled. In other words, for a 5% 3 σ (i.e., 15%) uncertainty on the planet mass and radius, the interior composition in terms of fractional composition of iron, silicates, and water cannot be determined. The reason this example fills almost the whole ternary diagram is that a planet with 10 $M_\oplus$ and 2 $R_\oplus$ has an average density in between two extreme cases (purely iron or purely water). Therefore, a large variety of different combinations of iron, silicate, and water can result in a similar M_p and R_p. Even taking a 1 σ uncertainty of the planet mass and radius, the uncertainty in internal composition is large.

We note that an uncertainty in R_p has more of an effect on the uncertainty in the interior composition than an uncertainty in M_p. This is because the planet's average density $\rho \sim M_p/R^3$. Considering error propagation, the uncertainty in radius has a 3 times larger effect on the uncertainty in average density than does the mass uncertainty.

We show ternary diagrams for planets with various masses, radii, and 5% fractional uncertainty in Figure 5. Only solutions
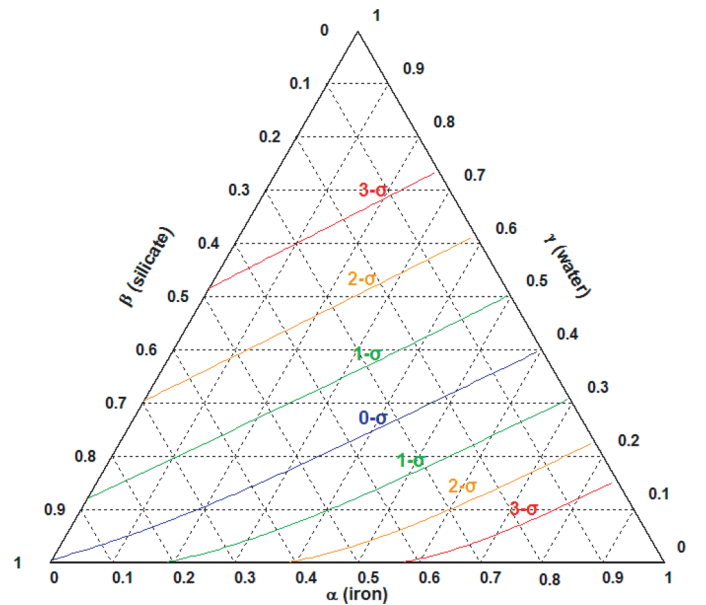

FIG. 4.—Ternary diagram including the mass and radius uncertainties for a planet of a fixed mass and radius. This example is for a planet with $M_p = 10 \pm 0.5\ M_\oplus$ and $R_p = 2 \pm 0.1\ M_\oplus$, showing the 1, 2, and 3 σ uncertainty curves. This Figure shows the continuous distribution of possible combinations of iron, silicate, and water with increasing uncertainties according to the color bar. Notice that considering the 3 σ uncertainties almost the entire ternary diagram is covered—in other words there is no constraint on the planet internal composition. See text for a discussion of the direction and spacing of the curves.
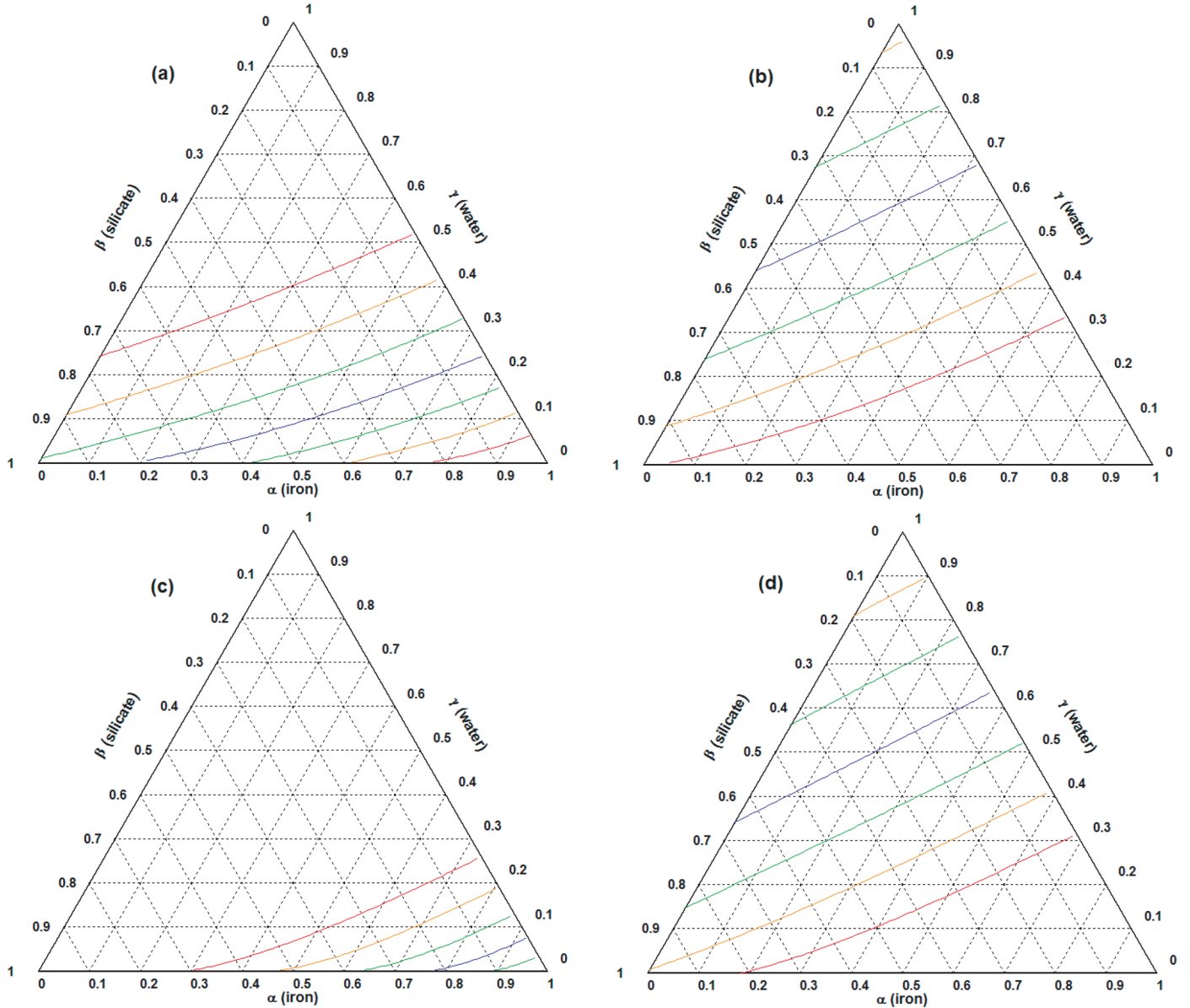
Fig. 5.—Ternary diagrams including 5% mass and radius uncertainties for planets of fixed mass and radius: *(a)* $M_p = 1 \pm 0.05\ M_\oplus$ and $R_p = 1 \pm 0.05\ M_\oplus$; *(b)* $M_p = 2 \pm 0.1\ M_\oplus$ and $R_p = 1.5 \pm 0.075\ M_\oplus$; *(c)* $M_p = 8 \pm 0.4\ M_\oplus$ and $R_p = 1.5 \pm 0.075\ M_\oplus$; and *(d)* $M_p = 16 \pm 0.8\ M_\oplus$ and $R_p = 2.5 \pm 0.125\ M_\oplus$. See text for a discussion of the direction and spacing of the curves.

in part of the ternary diagram are allowed, despite considering the $3\ \sigma$ range. In Figure 5b, the upper $3\ \sigma$ boundary is absent because it goes below the lowest allowed density of the $2\ M_\oplus$ and $1.5\ R_\oplus$ planet and is, thus, unphysical. In Figure 5c we see the opposite case, where the lower $3\ \sigma$ boundary is absent because it goes above the highest planet density allowed and is, thus, unphysical.

A ternary diagram for a fixed planet mass and radius that includes observational uncertainties is one of the primary outcomes of this paper.

4.2. Model Uncertainties

The model and computer code we present assumes a differentiated planet composed of an iron core, a silicate mantle, and a water–ice outer layer. The division into three major materials is based on the point that differences in the densities of iron, silicate, and water from each other are greater than any minor compositional variant of each individual material. The model neglects phase variation and temperatures, which, as argued in Seager et al. (2007), have little effect on the total planet radius

(to an uncertainty of about 1 to 3% uncertainty in planet radius, decreasing with increasing planet mass).

Low-pressure phase changes (at <10 GPa) are not important for a planet's radius because for plausible planet compositions most of the mass is at high pressure. For high pressure phase changes we expect the associated correction to the equation of state (and hence derived planet radii) to be small because at high pressure the importance of chemical bonding patterns to the equation of state drops.

Regarding temperature, at low pressures (≲10 GPa) in the outer planetary layers, the crystal lattice structure dominates the material's density and the thermal vibration contribution to the density are small in comparison. At high pressures the thermal pressure contribution to the EOS is small because the close-packed nature of the materials prevents structural changes from thermal pressure contributions.

Although the code can model radii for planets in the mass range 0.5 to 20 $M_\oplus$, the model is more accurate for planets above a few Earth masses (Seager et al. 2007).

The model also neglects variation in composition, such as a light element in the iron core as Earth and Mercury are believed to have. The model also omits other impurities in the mantle and water layer, including iron in the mantle. Molten cores have also been omitted. At the present time, these model uncertainties are expected to have an effect on the planet radius much less than the ~5% radius observational uncertainty.

For all of the above reasons, we therefore argue that for the present time the observational uncertainties dominate the model uncertainties; the model presented here is adequate for an estimate of planet bulk composition. In any event, the main results of our work are described in the following subsections despite any model uncertainties.

It is possible to rule out parts of the ternary diagram as being physically unplausible (e.g., Valencia et al. 2007). This is based on the initial composition of the protoplanetary nebula and on planet differentiation. For example, a pure iron planet is unlikely to exist, because removing all of the mantle would be difficult. A pure water planet is also unlikely to exist. Where water–ice forms, so do silicate-rich and iron-rich materials, making planet accretion of pure water unlikely. We prefer to leave the omission of parts of the ternary diagram to users of the code, because in exoplanets surprising exceptions to the "rules" of planet characteristics are not uncommon.

4.3. Spacing, Shape, Direction, and Rotation of Curves on the Ternary Diagram

We now turn to a discussion of the spacing, direction, and shape of the curves in the ternary diagrams. A quantitative and qualitative description of these is a main point of this paper. We emphasize that each curve in the diagrams shown in Figure 5 represents a different mass and radius. The curves to the lower right are more dense, as they have a higher mass and lower radius than the curves moving to the upper left.

All behavior results from the equations of state of the materials, and, in some cases, how they behave differently under pressure.

We begin with an equation that we use repeatedly in this section. We consider the simplified case that the planet core has a uniform density, where $\bar{\rho}_{\text{Fe}}$ is the average density of Fe in the core, $\bar{\rho}_{\text{MgSiO}_3}$ is the average density of silicate in the mantle, and $\bar{\rho}_{\text{H}_2\text{O}}$ is the average density of water in the outer water layer. We then have

$$\frac{4}{3}\pi R_p^3 = \left[\frac{\alpha M_p}{\bar{\rho}_{\text{Fe}}} + \frac{\beta M_p}{\bar{\rho}_{\text{MgSiO}_3}} + \frac{\gamma M_p}{\bar{\rho}_{\text{H}_2\text{O}}}\right], \tag{6}$$

where $\alpha + \beta + \gamma = 1$.

4.3.1. Spacing

The isomass-isoradius curves for adjacent curves with equal differences of mass and radius have uneven spacing on a ternary diagram. This spacing is generally smaller in the lower right part of the ternary diagram (high iron fraction region) than in the upper left part (high silicate or water fraction region). The curves in the lower right part of the diagram have a higher density (higher mass and smaller radius) than the curves found on the upper left part of the diagram. The density is not a linear function of both mass and radius; hence, we do not expect equal spacing on the ternary diagram. We can, however, give both a quantitative and qualitative explanation of the uneven spacing.

We can provide a quantitative description, beginning with equation (6), but using $\alpha = 1 - \beta - \gamma$ to get

$$\frac{4}{3}\pi R_p^3 = M_p\left[\frac{(1-\beta-\gamma)}{\bar{\rho}_{\text{Fe}}} + \frac{\beta}{\bar{\rho}_{\text{MgSiO}_3}} + \frac{\gamma}{\bar{\rho}_{\text{H}_2\text{O}}}\right]. \tag{7}$$

We use the fact that the curves on the ternary diagram are almost perpendicular to the water side of the ternary diagram, and therefore set the silicate mass fraction $\beta = 0$ for our discussion. In other words, the distance (separation) between the points produced by the intersection of the isomass-isoradius curves and the water axis is a good representation of the spacing between the curves throughout the ternary diagram,

$$\frac{4}{3}\pi R_p^3 = M_p\left[\frac{1}{\bar{\rho}_{\text{Fe}}} + \gamma\left(\frac{1}{\bar{\rho}_{\text{H}_2\text{O}}} - \frac{1}{\bar{\rho}_{\text{Fe}}}\right)\right]. \tag{8}$$

We define the following constants:

$$A_1 = \frac{1}{\bar{\rho}_{\text{Fe}}} \tag{9}$$

and

$$A_2 = \frac{1}{\bar{\rho}_{\text{H}_2\text{O}}} - \frac{1}{\bar{\rho}_{\text{Fe}}}. \tag{10}$$

Equation (8) then becomes

$$\gamma A_2 = \frac{4/3\pi R_p^3}{M_p} - A_1. \qquad (11)$$

We note that $A_1 > 0$ and $A_2 > 0$.

Now we proceed to take the derivative of equation (11) with respect to the change of mass (dM_p) and change of radius (dR_p).

$$A_2 d\gamma = \frac{4\pi}{3}\left[\frac{3R_p^2}{M_p}dR_p - \frac{R_p^3}{M_p^2}dM_p\right]. \qquad (12)$$

We can also rewrite equation (11) in terms of the overall average density of the planet ($\bar\rho$)

$$\gamma A_2 = \frac{1}{\bar\rho} - A_1, \qquad (13)$$

and the corresponding derivative relative to the overall average density ($\bar\rho$)

$$A_2 d\gamma = -\frac{1}{\bar\rho^2} - d\bar\rho. \qquad (14)$$

This leads to our quantitative understanding, where we first recall that $d\gamma$ is the water fraction spacing on the ternary diagram. The lower right part (Fe-rich) of the ternary diagram is where the average density ($\bar\rho$) of a planet is high. This implies that (for the same $d\bar\rho$) $d\gamma$ is small (since $\bar\rho$ is in the denominator). In the upper left region of the ternary diagram (water-rich) the average planet density is smaller than a planet located in the lower right part of the diagram, and, therefore, $d\gamma$ is larger.

Qualitatively, to have wider spacing an increasing water fraction is needed. In other words, toward the upper right part of the ternary diagram, for the same density difference more water than iron must be replaced.

We note that the spacing is predominantly the result of the nonlinearity of equations (11)) and (14) and the average density of each compositional layer, not of any P-ρ properties of the EOS (i.e., how materials condense under high pressure). This statement is correct under the assumption of a single material for each layer in the planet (in our case for iron, silicate, and water). The assumption that the average density within each layer does not change significantly from curve to curve (for example, from the 1 σ curve to the 3 σ curve for the case $M_p = 2\,M_\oplus$ and $R_p = 1.5\,R_\oplus$) is reasonable for a ternary diagram that spans only a small mass and radius range.

4.3.2. Shape, Direction, and Rotation

To explain the shape and direction of the curves in the ternary diagrams, we start by explaining the slope of the curves in the

Cartesian diagram. In other words, we are aiming for an expression of $d\alpha/d\beta$.

We start with a different form of equation (6),

$$\alpha\left[\frac{1}{\bar\rho_{H_2O}} - \frac{1}{\bar\rho_{Fe}}\right] + \beta\left[\frac{1}{\bar\rho_{H_2O}} - \frac{1}{\bar\rho_{MgSiO_3}}\right] = \frac{1}{\bar\rho_{H_2O}} - \frac{4\pi R_p^3}{3M_p}. \quad (15)$$

We now differentiate this equation with respect to α and β to find

$$d\alpha\left[\frac{1}{\bar\rho_{H_2O}} - \frac{1}{\bar\rho_{Fe}}\right] + d\beta\left[\frac{1}{\bar\rho_{H_2O}} - \frac{1}{\bar\rho_{MgSiO_3}}\right] \approx 0, \qquad (16)$$

based on the assumption that the average density is changing slowly with respect to the change in composition.

We write the slope of the curves in the Cartesian diagram

$$\left|\frac{d\beta}{d\alpha}\right| = \frac{\left[1 - \frac{\bar\rho_{H_2O}}{\bar\rho_{Fe}}\right]}{\left[1 - \frac{\bar\rho_{H_2O}}{\bar\rho_{MgSiO_3}}\right]}. \qquad (17)$$

We can see that

$$\left|\frac{d\beta}{d\alpha}\right| > 1, \qquad (18)$$

assuming that $\bar\rho_{H_2O} < \bar\rho_{MgSiO_3} < \bar\rho_{Fe}$.

It can be shown that the slope in the ternary diagram has a positive connection to the slope in the Cartesian diagram. Using the equations that convert the Cartesian coordinates to coordinates on the ternary diagram (eqs. [3] and [4]), we find that

$$\left|\frac{d\beta_{\text{ternary}}}{d\alpha_{\text{ternary}}}\right| = \sqrt{3}\frac{\left[\left|\frac{d\beta}{d\alpha}\right| - 1\right]}{\left[\left|\frac{d\beta}{d\alpha}\right| + 1\right]}. \qquad (19)$$

We can now go on to describe the direction, shape, and rotation in the Cartesian diagram based on equation (17) with the knowledge that the same qualitative behavior will appear in the ternary diagrams. We first emphasize that the slope of an iso-mass-isoradius curve on the ternary diagram describes adding and removing mass of the different species.

We begin with a qualitative explanation of the direction of the curves on the ternary diagram—why each curve goes from the lower left to the upper right. This is largely a coincidence in the different values of $\bar\rho_{H_2O}$, $\bar\rho_{MgSiO_3}$, and $\bar\rho_{Fe}$. The coincidence lies in the fact that iron is more dense than silicate and water is less dense—and for zero-pressure densities, an equal mass of iron and water combined densities are roughly similar to the silicate density. At the lower left of the ternary diagram in Figure 3, the silicate mass fraction is 80%, the iron mass fraction

is zero and the water mass fraction is 20%. As the silicate fraction decreases, a combination of equal parts iron and water must be added to maintain the same overall planet mass and radius. This description is consistent with the direction of the curves in the ternary diagrams.

More quantitatively, from equation (17), we can take the zero-pressure densities of Fe, H_2O, and $MgSiO_3$ to find the slope of the curve on the Cartesian diagram

$$\left| \frac{d\beta}{d\alpha} \right| = 2 \tag{20}$$

and from equations (3) and (4)

$$\left| \frac{d\beta_{\text{ternary}}}{d\alpha_{\text{ternary}}} \right| = \frac{1}{\sqrt{3}}. \tag{21}$$

We can consider removing a fixed amount of iron mass, e.g., 1 g. According to equation (20), 2 g of silicate must be added. For mass balance (because each curve on the ternary diagram represents a planet of fixed mass and fixed radius), 1 g of water must be removed. The direction of the curves on the ternary diagram do correspond to removing roughly equal masses of iron and water for every mass of silicate added.

4.3.2.1 Rotation

In Figures 5a, 5b, 5c, and 5d (where a through d are in order of increasing mass), we see that for more massive planets, the isomass-isoradius curves are rotated. In other words, the slope of the curve on the ternary diagram increases for increasing mass.

We again return to equation (17). With increasing planet mass, $\bar{\rho}_{H_2O}$, $\bar{\rho}_{MgSiO_3}$, and $\bar{\rho}_{Fe}$ each change. Because iron is in the core, it suffers more compression than the silicate mantle or water-ice layer. In other words, $\bar{\rho}_{Fe}$ must increase more than $\bar{\rho}_{H_2O}$ and $\bar{\rho}_{MgSiO_3}$ as the planet mass increases. Therefore, the numerator of equation (17) gets larger and thus the slope of the curve increases. The rotation is counter clockwise with increase of mass.

4.3.2.2 Slope of the Curves

We now turn to discuss the slope of each isomass-isoradius curve. We see from Figures (4) and (5) that the slope of each isomass-isoradius curve for a fixed mass and radius is greater in the lower left part of the curve than in the upper right part of the curve.

The slope is due to the differential compression of water, silicate, and iron under pressure. This slope is again explained by equation (17). At the lower left, the slope is smaller; this is the silicate-rich region of the ternary diagram. There is more silicate and less iron and water. The $\bar{\rho}_{MgSiO_3}$ will increase as it gets compressed in the inner part of the planet. This causes the slope in equation (17) to get smaller. In contrast, at the upper right, there is little silicate, but more water and iron. The silicate

and water are less compressed, but the iron is more compressed, making the slope increase.

For a conceptual explanation, first recall the idea described above that removing 2 g of silicate can be compensated for by adding approximately 1 g of water and 1 g of iron. In a silicate-rich planet (lower left of the ternary diagram), silicate is compressed. For a massive planet, this compression makes the silicate density closer to iron's density than when compared in the uncompressed case. Therefore, removing a fixed mass of silicate requires much more iron than water to be added, for a fixed mass and radius.

In contrast, along the upper right part of the ternary diagram, the planet is iron rich or water rich. The slope of an isomass-isoradius curve is steeper than a curve in the lower left part of the ternary diagram. For an isomass-isoradius curve in the upper part of the ternary diagram, the planet has more iron, and the iron is very compressed. (There is less silicate and the silicate is, overall, less compressed compared to a planet in the lower left of the ternary diagram.) If a fixed mass of silicate is removed, more water than iron must be added to compensate for the density of compressed iron. The density of water does not change much, because water is always the outer layer and thus the least compressed.

As a qualitative explanation, if the average density of each of the three layers remains constant, then an isomass-isoradius curve should always be a straight line in either the Cartesian or ternary representation. The curvature in a given isomass-isoradius curve appears because of the compression of material under pressure, which is a property of the EOS.

4.4. Shape and Direction of an Isoradius Surface in our 3D Representation

We return to the 3D representation of the relationship between mass, radius, and composition shown in Figure 1. An isoradius surface (red oblique surface) is shown for $R_p = 1.7\ R_\oplus$. An isomass surface (one of the blue flat planes) is shown for $M_p = 4\ M_\oplus$. At the bottom tip of the isoradius surface the silicate mass fraction = iron mass fraction = 0, and the planet is composed of 100% water. This is the minimum mass for this radius. The isoradius surface also has a maximum mass reached by a composition of 100% iron.

For the same radius, if either the silicate or iron mass fraction is increased, the planet mass must also increase. This is because iron and silicate are denser than water–ice. We further note that for an increase in the iron mass fraction, the mass of the planet must increase more steeply than for an increase in the silicate mass fraction. This is seen by the different length and shape of the "edges" of the isomass surface in the iron-mass plane and silicate-mass plane in Figure 1.

We now show that the shape of the isoradius surface is concave. The isoradius surface can be considered as the isovolume surface, where the volume is the sum of the core, the silicate mantle, and the water crust. To calculate the total mass of a point

on the isoradius curve, we use equation (6), and since R_p is constant on this surface we can rewrite this equation (with C a constant) as,

$$M_p = C\left[\frac{\alpha}{\bar{\rho}_{\mathrm{Fe}}} + \frac{\beta}{\bar{\rho}_{\mathrm{MgSiO_3}}} + \frac{(1-\alpha-\beta)}{\bar{\rho}_{\mathrm{H_2O}}}\right]^{-1}. \qquad (22)$$

The term in brackets is a linear function and its inverse is hyperbolic. For example, if we let $\alpha = 0$ (no iron), then we have

$$M_p = C\left[\frac{1}{\bar{\rho}_{\mathrm{H_2O}}} - \beta\left(\frac{1}{\bar{\rho}_{\mathrm{H_2O}}} - \frac{1}{\bar{\rho}_{\mathrm{MgSiO_3}}}\right)\right]^{-1}, \qquad (23)$$

where

$$C = \frac{4}{3}\pi R_p^3. \qquad (24)$$

Both terms in the square brackets are positive and $0 \le \beta \le 1$. This is in the form

$$M_p = \frac{C}{C_1 - C_2\beta}, \qquad (25)$$

where

$$C_1 = \frac{1}{\bar{\rho}_{\mathrm{H_2O}}} \qquad (26)$$

and

$$C_2 = \frac{1}{\bar{\rho}_{\mathrm{H_2O}}} - \frac{1}{\bar{\rho}_{\mathrm{MgSiO_3}}}. \qquad (27)$$

We have $C_1 > C_2 > 0$. This is the form of a concave hyperbola, because, taking the first derivative, we find

$$\frac{dM_p}{d\beta} = \frac{CC_2}{(C_1 - C_2\beta)^2}. \qquad (28)$$

The slope increases as β increases because $C_1 - C_2\beta$ decreases but is always greater than zero.

Although we have made the simplification that the average densities of each layer remain constant, our qualitative description holds because $\bar{\rho}_{\mathrm{H_2O}} < \bar{\rho}_{\mathrm{MgSiO_3}} < \bar{\rho}_{\mathrm{Fe}}$ as long as the planet is differentiated into layers of increasing density toward the planet center.

A similar argument shows that the total iron fraction versus the total mass is also a hyperbola, making the whole isoradius surface concave.

5. SUMMARY AND CONCLUSION

An ambiguity in an exoplanet interior composition remains for any planet with a measured mass and radius, no matter how precisely measured. We can accept this ambiguity and quantify it with the aid of ternary diagrams (Valencia et al. 2007). We have presented ternary diagrams for a single planet of fixed mass and radius, for a planet composed of an iron core, a silicate mantle, and a water–ice outer layer. Our ternary diagram presentation includes observational uncertainties. We have provided a publicly available computer code to generate a ternary diagram for a given input mass, radius, and observational uncertainties.

In addition to presenting ternary diagrams for fixed mass and radius, we showed their origin from a 4D database (M_p, R_p, iron mass fraction α, and the silicate-mass fraction β; recall that the water–ice mass fraction $\gamma = 1 - \alpha - \beta$). We further described the shape and direction of the composition curves on a ternary diagram.

We conclude with the sentiment that in order to fully understand the interior structure of an exoplanet, a third measurement beyond planet mass and radius is required.

REFERENCES

Fortney, J. J., Marley, M. S., & Barnes, J. W. 2007, ApJ, 659, 1661

Seager, S., Kuchner, M., Hier-Majumder, C. A., & Militzer, B. 2007, ApJ, 669, 1279

Selsis, F., et al. 2007, Icarus, 191, 453

Sotin, C., Grasset, O., & Mocquet, A. 2007, Icarus, 191, 337

Stevenson, D. J. 1982, Planet. Space Sci., 30, 755

Valencia, D., O'Connell, R. J., & Sasselov, D. 2006, Icarus, 181, 545

Valencia, D., Sasselov, D. D., & O'Connell, R. J. 2007, ApJ, 665, 1413

Zapolsky, H. S., & Salpeter, E. E. 1969, ApJ, 158, 809